Research Article

Nano Research
2024, 17(3): 1508–1515

ISSN 1998-0124 CN 11-5974/O4
https://doi.org/10.1007/s12274-023-5981-7

Antimony doped $CsPbI_2Br$ for high-stability all-inorganic perovskite solar cells

Mengfei Zhu[1,§], Lina Qin[1,§], Yuren Xia[1,§], Junchuan Liang[1], Yaoda Wang[1], Daocheng Hong[1], Yuxi Tian[1], Zuoxiu Tie[1,2,3] (✉), and Zhong Jin[1,2,3] (✉)

[1] *State Key Laboratory of Coordination Chemistry, Ministry of Education (MOE) Key Laboratory of Mesoscopic Chemistry, MOE Key Laboratory of High Performance Polymer Materials and Technology, Jiangsu Key Laboratory of Advanced Organic Materials, School of Chemistry and Chemical Engineering, Nanjing University, Nanjing 210023, China*
[2] *Nanjing Tieming Energy Technology Co., Ltd., Nanjing 210093, China*
[3] *Suzhou Tierui New Energy Technology Co., Ltd., Suzhou 215228, China*
[§] *Mengfei Zhu, Lina Qin, and Yuren Xia contributed equally to this work.*

Received: 5 May 2023 / **Revised:** 27 June 2023 / **Accepted:** 4 July 2023

ABSTRACT

All-inorganic perovskites, adopting cesium (Cs^+) cation to completely replace the organic component of A-sites of hybrid organic–inorganic halide perovskites, have attracted much attention owing to the excellent thermal stability. However, all-inorganic iodine-based perovskites generally exhibit poor phase stability in ambient conditions. Herein, we propose an efficient strategy to introduce antimony (Sb^{3+}) into the crystalline lattices of $CsPbI_2Br$ perovskite, which can effectively regulate the growth of perovskite crystals to obtain a more stable perovskite phase. Due to the much smaller ionic radius and lower electronegativity of trivalent Sb^{3+} than those of Pb^{2+}, the Sb^{3+} doping can decrease surface defects and suppress charge recombination, resulting in longer carrier lifetime and negligible hysteresis. As a result, the all-inorganic perovskite solar cells (PSCs) based on 0.25% Sb^{3+} doped $CsPbI_2Br$ light absorber and screen-printable nanocarbon counter electrode achieved a power conversion efficiency of 11.06%, which is 16% higher than that of the control devices without Sb^{3+} doping. Moreover, the Sb^{3+} doped all-inorganic PSCs also exhibited greatly improved endurance against heat and moisture. Due to the use of low-cost and easy-to-process nanocarbon counter electrodes, the manufacturing process of the all-inorganic PSCs is very convenient and highly repeatable, and the manufacturing cost can be greatly reduced. This work offers a promising approach to constructing high-stability all-inorganic PSCs by introducing appropriate lattice doping.

KEYWORDS

all-inorganic perovskite solar cells, Sb doped cesium lead halide perovskites, foreign B-site ions, hole-conductor-free, phase stability improvement

1 Introduction

Organic–inorganic hybrid perovskite solar cells (PSCs) have attracted widespread attention in the field of photovoltaic research [1–4]. Since 2009, the photo-conversion efficiency (PCE) of PSCs has increased from 3.8% to 25.7% [5–7]. However, the stability, especially the thermal durability of PSCs, is still unsatisfactory [8]. The A-sites of lead halide perovskites usually contain methylammonium (MA^+) or formamidine (FA^+), which are organic components with poor heat tolerance [9–11]. One effective way to improve the stability of PSCs is to partially or completely replace MA^+ and FA^+ with Cs^+ [12–14]. All-inorganic Cs-based perovskites are more stable at high temperatures, but the Cs-based perovskites might degrade into other phases without photo-activity at room temperature [15]. To stabilize the effective crystalline phase of the all-inorganic perovskites, Br^- could be incorporated into X-sites, since Br-based perovskites have better stability than I-based perovskites [16]. Pristine $CsPbBr_3$ exhibits good stability, but its band gap is wide (~ 2.3 eV), which is not conducive to the absorption of sunlight [17, 18]. While $CsPbI_3$ has a smaller band gap (~ 1.7 eV), the stability is not ideal [19, 20]. Therefore, $CsPbI_2Br$ can be used as a compromise perovskite material that balances the light absorption performance and operation stability [21–23]. On the other hand, introducing foreign metal ions into the B-sites of perovskites also can improve the stability. For instance, researchers have doped Zn^{2+}, Sr^{2+}, Mn^{2+}, and In^{3+} into the lattices of $CsPbI_2Br$ perovskite, obtaining a more stable inorganic perovskite phase and favorable photovoltaic performance [24–27]. However, the hygroscopic nature of their iodide poses a potential risk to the long-term stability of the devices when exposed to damp air. As a trivalent main-group metal ion, the Sb^{3+} with a small radius has a similar electronic structure to Pb^{2+}, and its iodide exhibits excellent moisture resistance. Sb-based dopants are promising to be introduced into the B-sites of $CsPbI_2Br$ perovskite for enhancing the optical and electronic properties. Moreover, the presence of labile organic hole transport materials (HTMs) in PSCs is also unfavorable to the operation stability. Aiming to stabilize the entire device, some inorganic materials such as NiO_x could be used as HTMs [28], or

Address correspondence to Zuoxiu Tie, zxtie@nju.edu.cn; Zhong Jin, zhongjin@nju.edu.cn

a carbon electrode could simultaneously act a bi-functional role of both HTM and current collector [29, 30].

Herein, we report the introduction of Sb^{3+} into the crystal lattices of $CsPbI_2Br$ perovskite, and meanwhile a low-cost and screen-printable nanocarbon electrode is used to replace organic HTMs and expensive noble metal counter electrodes. As thus, HTM-free all-inorganic PSCs with a structure of fluorine-doped tin oxide (FTO)/c-TiO_2/m-TiO_2/perovskite/nanocarbon were fabricated. Since Sb^{3+} has a much smaller ionic radius and lower electronegativity than Pb^{2+}, the incorporation of Sb^{3+} could effectively change the crystallization behavior and stabilize the lattice phase of $CsPbI_2Br$ films, thus greatly enhancing the phase stability of the perovskites. With an Sb doping ratio of 0.25%, the PCE of the all-inorganic PSCs can reach 11.06%, superior to that of the undoped devices (9.55%). More importantly, the all-inorganic PSCs based on Sb-doped $CsPbI_2Br$ exhibited greatly enhanced thermal and humid stabilities, attributing to a more suitable tolerance factor of Sb^{3+} dopant.

2 Results and discussion

The Sb-doped $CsPbI_2Br$ perovskite films were prepared by a one-step spin-coating approach using CsI, $PbBr_2$, PbI_2, and SbI_3 precursors dissolved in dimethyl sulfoxide (DMSO), as detailed in the Methods section in the Electronic Supplementary Material (ESM). The crystal structure of all-inorganic perovskite $CsPbI_2Br$ doped with Sb^{3+} is shown in Fig. 1(a), where the A-sites are occupied by Cs^+ cations, the B-sites are occupied by metal ions (Pb^{2+} or Sb^{3+}), and the X-sites are occupied by I^- and Br^- ions with a ratio of 2:1. The as-prepared all-inorganic perovskite films, including pristine $CsPbI_2Br$, 0.25%-Sb $CsPbI_2Br$, and 1%-Sb $CsPbI_2Br$, were characterized by X-ray diffraction (XRD) to study the effect of Sb substitution on the crystallinity (Fig. 1(b)). The XRD peaks of all the as-prepared samples located at 14.6° and 29.5° are assigned to the (100) and (200) planes of cubic $CsPbI_2Br$, respectively [31]. However, there are still some differences between the samples. The 0.25%-Sb $CsPbI_2Br$ sample has the highest (200) peak intensity. By comparing the full width half maximum (FWHM) of the main (200) peaks of these samples (0%-Sb: 0.22°, 0.25%-Sb: 0.21°, and 1%-Sb: 0.27°), it is found that the 0.25%-Sb $CsPbI_2Br$ sample has the lowest FWHM value, indicating its highly ordered crystal structure. Besides, the pristine $CsPbI_2Br$ film has an additional diffraction peak at 20.9°, which corresponds to the (110) planes of cubic $CsPbI_2Br$. The obvious (110) diffraction peak of the pristine sample indicates its inferior crystal growth alignment and lower crystallinity degree. As shown in Fig. S1 in

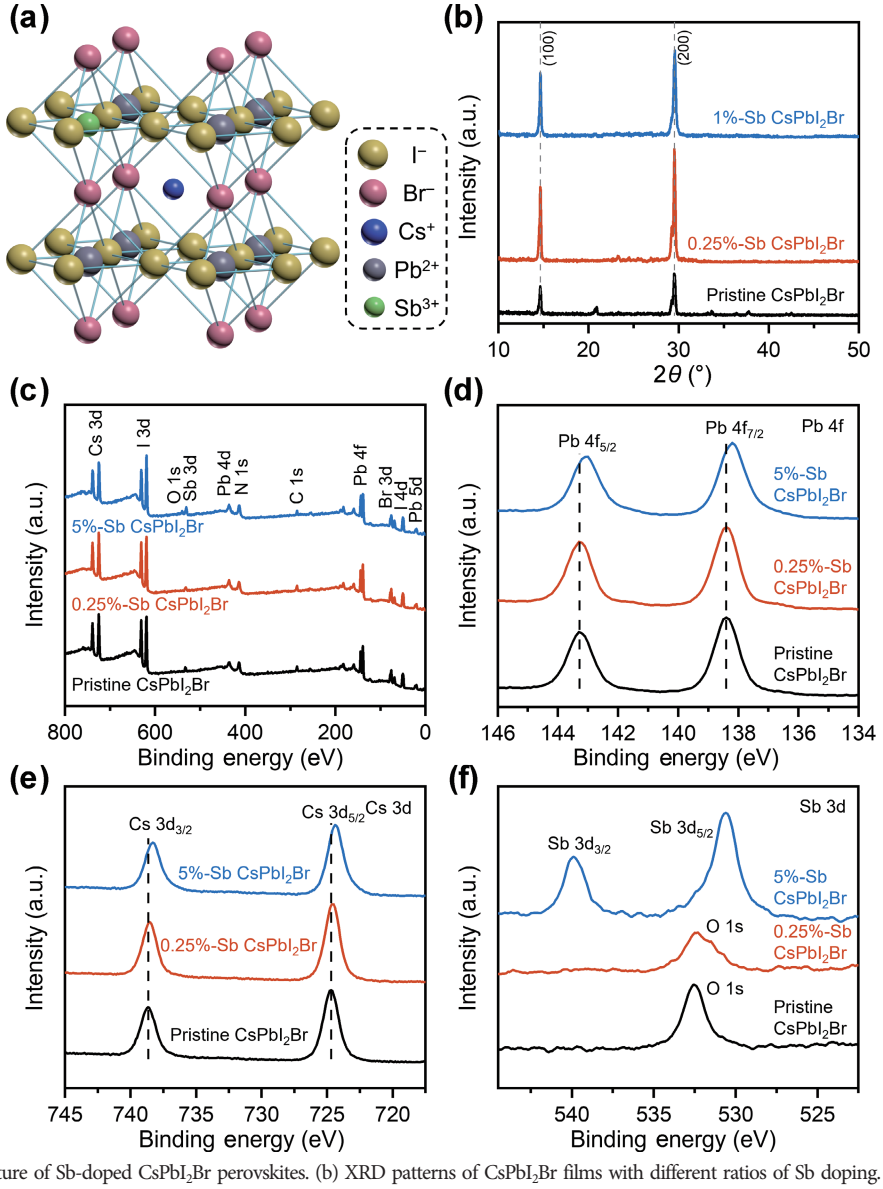

Figure 1 (a) Crystal structure of Sb-doped $CsPbI_2Br$ perovskites. (b) XRD patterns of $CsPbI_2Br$ films with different ratios of Sb doping. (c) XPS spectra of pristine $CsPbI_2Br$ (black line), 0.25%-Sb $CsPbI_2Br$ (red line), and 5%-Sb $CsPbI_2Br$ (blue line) films. High-resolution XPS spectra of the samples at (d) Pb 4f, (e) Cs 3d, and (f) Sb 3d regions, respectively.

the ESM, the (200) diffraction peaks of the samples slightly shift to higher angles, indicating a decrease in the lattice constants due to the introduction of Sb^{3+} ions. These results indicate that a proper amount of Sb doping could decrease the crystal defects and enhance the crystallinity of perovskite films, which is conducive to the transport of photo-generated carriers in the perovskite films. When the Sb-doping ratio further increases, the intensities of the (100) and (200) peaks gradually decrease, and the intensity of the (110) diffraction peak gradually increases (Fig. S2 in the ESM). Especially, when the Sb-doping ratio increases to a high level (5% and 10%), the intensities of the (100) and (200) peaks are significantly decreased, and an obvious impurity peak appears at 25.5°, which is attributed to the (101) planes of anatase TiO_2. The (101) peak of TiO_2 becomes the main peak at the Sb-doping ratio of 10%, suggesting a very low crystallinity. This suggests that the foreign Sb^{3+} ions have a great influence on the crystallization process of $CsPbI_2Br$ film. Briefly, a moderate Sb-doping ratio is beneficial to improving the crystal quality, while an excessively high doping ratio over the threshold will decrease the crystalline degree of perovskite film.

X-ray photoelectron spectroscopy (XPS) analysis results of pristine $CsPbI_2Br$, 0.25%-Sb $CsPbI_2Br$, and 5%-Sb $CsPbI_2Br$ films are shown in Fig. 1(c). The high-resolution XPS spectra at Pb 4f, Cs 3d, Sb 3d, I 3d, and Br 3d regions are also compared in Figs. 1(d)–1(f), and Fig. S4 in the ESM, and the characteristic binding energies of these elements are summarized in Table S1 in the ESM. The presence of two binding energy peaks near 535 eV is attributed to the Sb 3d core levels, which confirms the existence of Sb^{3+}. Specifically, the two peaks at 530.6 and 539.9 eV are indexed to Sb $3d_{5/2}$ and Sb $3d_{3/2}$ bands, respectively (Fig. 1(f)). In the 0.25%-Sb $CsPbI_2Br$ sample, the Sb 3d peaks are very weak, because the atomic percentage of Sb is very low and barely detected. The high-resolution XPS spectrum at Sb 3d region of 1%-Sb $CsPbI_2Br$ film is also presented in Fig. S3 in the ESM. However, the shifts of Cs 3d and I 3d peaks prove that Sb^{3+} has been introduced into the perovskite film (Fig. 1(e), and Fig. S4(a) and Table S1 in the ESM). Notably, compared to pristine $CsPbI_2Br$, all the XPS peaks of Sb-doped $CsPbI_2Br$ samples shift to lower binding energy levels, which is attributed to the doping effect of Sb^{3+} ions and the resulting change of chemical bonds. It is known that Sb has a lower electronegativity (2.05) compared with Pb (2.33). In Sb-doped samples, the binding energy of Pb 4f with halide ions is decreased due to the strong chemical interaction between Sb^{3+} and X^- (X = Cl, Br, or I). Meanwhile, Sb is more likely to lose valence electrons, while other atoms such as Cs, I, and Br in the perovskite crystal tend to get valence electrons and thus reduce the binding energy of these atoms. In addition, the energy-dispersive X-ray (EDX) spectroscopy elemental mappings in Fig. S5 in the ESM show that Sb is uniformly distributed in the 1%-Sb $CsPbI_2Br$ sample. Similarly, Sb is barely detected in the 0.25%-Sb $CsPbI_2Br$ film by EDX because the content of Sb atoms is almost below the detection limit.

The morphology features of pristine $CsPbI_2Br$ and Sb-doped $CsPbI_2Br$ films were studied by scanning electron microscopy (SEM) (Fig. 2(a)). In comparison to the pristine $CsPbI_2Br$ film, the 0.25%-Sb $CsPbI_2Br$ film demonstrates a reduced number of pinholes and a more uniform morphology, primarily due to its improved crystal orientation consistency [32]. However, when the Sb doping content is increased to 1%, the number of pinholes increases once again due to decreased crystallinity, which is consistent to the findings from the XRD analysis. These pinholes could hinder the transport of electrons and holes and increase the recombination of them, thereby affecting the photovoltaic performance of PSCs. Additionally, the doping of Sb^{3+} ions with a small radius into $CsPbI_2Br$ perovskite results in a contracted lattice volume and enhanced phase stability, making it an effective stabilizer to maintain the α-phase seeds during the low-temperature annealing step. Upon annealing at 160 °C, the crystal seeds undergo complete growth, leading to a significant enhancement in the crystallinity and quality of the perovskite films. Hence, the utilization of Sb^{3+} was implemented to mitigate the occurrence of pinholes, reduce defect density, alleviate lattice strain, and subsequently enhance both the photovoltaic performance and stability [33, 34].

The effects of Sb^{3+} doping on the photo-physical properties were further studied (Fig. 2(b)). It can be found that as the content of Sb doping increases, the ultraviolet–visible (UV–Vis) absorption spectra appear blue shift. The blue shift of the absorption edge can be observed more clearly in the partially enlarged view (Fig. S6 in the ESM). The optical band gaps of the perovskite films were calculated based on the Tauc diagram converted from the UV–Vis absorption spectra (Fig. 2(c)) [35], and the corresponding band gap values are marked in the plot. With the increase of Sb-doping content from 0% to 1%, the optical band gap increases from 1.903 to 1.916 eV. Previous studies suggest that the incorporation of Sb may cause the enlargement of band gap due to the stronger Sb–X bonds [36, 37]. The photoluminescence (PL) spectra of pristine $CsPbI_2Br$, 0.25%-Sb $CsPbI_2Br$, and 1%-Sb $CsPbI_2Br$ films deposited on ordinary glass substrates were measured under an excitation wavelength of 450 nm (Fig. 2(d)). The 0.25%-Sb $CsPbI_2Br$ film exhibits an enhanced PL intensity, indicating highly improved photo-response properties. Conversely, excessive Sb doping results in the negative effect on PL intensity, which can be attributed to the reduction of photosensitive phase. As the Sb-doping ratio increases, a blue shift is observed with the emission peaks around 659, 656, and 646 nm, respectively, which is consistent with the measured optical band gaps in Fig. 2(c). The UV–Vis absorption spectrum and corresponding optical band gap of 10%-Sb $CsPbI_2Br$ film were also measured (Fig. S7 in the ESM), showing a band gap widening compared to the other samples. Theoretically, the valence band maximum (VBM) of ABX_3 perovskite is mainly composed of antibonding hybridization B *n*s and X *n*'p orbitals with main contribution from X *n*'p, while the minimum conduction band (CBM) is determined by the antibonding mixing of B *n*p and X *n*'p orbitals with dominant contribution from B *n*p [38]. On the contrary, the effects of A-site cations on VBM or CBM are negligible. Therefore, due to the additional I^- ions brought by SbI_3 relative to PbI_2, some of the Br^- ions in the crystal structure may be replaced by I^- ions, which makes the VBM move to a higher level. Meanwhile, the CBM value moves up because of the substitution of Pb^{2+} ions with Sb^{3+} ions. To determine the exact VBM values, the valence band XPS spectra of pristine $CsPbI_2Br$, 0.25%-Sb $CsPbI_2Br$, and 1%-Sb $CsPbI_2Br$ films were collected (Fig. 2(e)). The work function of the spectrometer used for XPS analysis is 4.5 eV (the binding energy of Ag 4d). By linearly extrapolating the valence band XPS curves, the VBM values of these three samples are determined as −5.68, −5.64, and −5.55 eV, respectively. Combining the optical band gap values of the samples obtained from the UV–Vis absorption spectra, the CBM values of the samples are calculated to be −3.78, −3.73, and −3.63 eV, respectively.

To better understand the influence of Sb doping on the photovoltaic performance, a series of all-inorganic PSCs based on screen-printable nanocarbon counter electrode and free of HTM were fabricated, with a structure of FTO/c-TiO_2/m-TiO_2/perovskite/nanocarbon (Fig. 3(a)). Among these all-inorganic PSCs, the unstable organic HTMs and expensive noble metal electrodes in traditional organic–inorganic hybrid PSCs are replaced by screen-printable nanocarbon electrodes with high stability, easy processability, and low cost. Moreover, nanocarbon electrode can effectively work for both hole extraction and

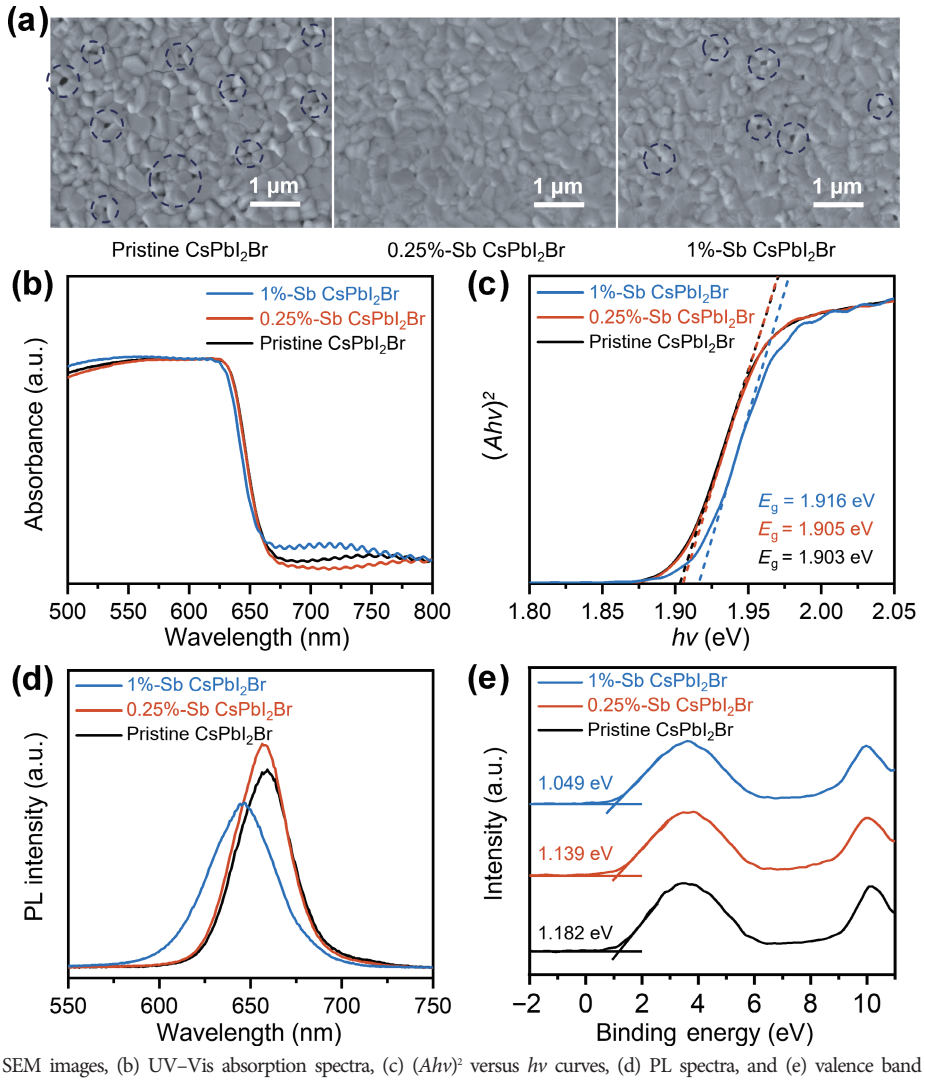

Figure 2 (a) Top-view SEM images, (b) UV–Vis absorption spectra, (c) $(Ahv)^2$ versus hv curves, (d) PL spectra, and (e) valence band XPS spectra of pristine $CsPbI_2Br$, 0.25%-Sb $CsPbI_2Br$, and 1%-Sb $CsPbI_2Br$ films, respectively.

collection, because it has a suitable work function (−5.0 eV) similar to gold (−5.1 eV). The cross-sectional SEM image of a typical device is shown in Fig. 3(b), and the thickness of inorganic perovskite film is approximately 500 nm. Figure 3(c) shows the energy band levels of HTM-free all-inorganic PSCs based on pristine and Sb-doped $CsPbI_2Br$ light absorber films. Due to the well-matched energy band levels, both the electron transport from the CBM of inorganic perovskite to c-TiO_2/m-TiO_2 layer, and the hole transport from the VBM of inorganic perovskite to nanocarbon electrode, could carry on favorably.

The photocurrent density–voltage (J–V) curves of all-inorganic PSCs based on $CsPbI_2Br$ films with varying amounts of Sb doping are shown in Fig. 3(d). And the corresponding photovoltaic parameters are summarized in Table S2 in the ESM, including open circuit voltage (V_{OC}), short-circuit current density (J_{SC}), fill factor (FF), PCE, and optical band gaps. The PCE of the HTM-free all-inorganic PSC based on undoped $CsPbI_2Br$ film achieved a PCE of 9.55%, with a V_{OC} of 1.097 V, a J_{SC} of 14.79 mA/cm^2, and an FF of 0.58. The devices based on 0.25%-Sb $CsPbI_2Br$ films exhibited the best performance, achieving a PCE up to 11.06%, which could be attributed to an increase in correlative photovoltaic parameters (V_{OC} = 1.146 V, J_{SC} = 15.71 mA/cm^2, and FF = 0.61). However, when the doping ratio was increased to 1%, the corresponding photovoltaic parameters of the device decreased, with a PCE of 7.95%, a V_{OC} of 1.035 V, a J_{SC} of 14.66 mA/cm^2, and an FF of 0.52. These results suggest that an Sb doping ratio of 0.25% is the optimal choice, as it leads to better crystallinity, film quality, and dense morphology, which in turn enable higher values of J_{SC} and V_{OC}. When 1% Sb was doped into the samples, a large number of pinholes were observed in the film which resulted in lower values for both V_{OC} and FF. The photovoltaic parameters of all-inorganic PSCs based on $CsPbI_2Br$ with varying Sb doping ratios are listed in Table S2 in the ESM. The results indicate that when the doping level is increased beyond 2%, the performance of the device deteriorates, particularly with a detrimental V_{OC} of less than 0.95 V, which can be attributed to electrical leakage. To verify the repeatability of the fabricated devices, a total of 20 individual all-inorganic PSCs based on 0.25%-Sb $CsPbI_2Br$ films were produced. The statistical histogram of the PCEs for these devices is presented in Fig. 3(e), and their photovoltaic parameters are summarized in Table S3 in the ESM. The narrow distribution of the PCE values, with an average value of 10.7% as shown in the histogram, indicates a high level of repeatability in device manufacturing. As indicated in Table S4 in the ESM, the 0.25%-Sb $CsPbI_2Br$-based PSCs in our work possess the highest PCE and current density record compared to previous literatures on other doped all-inorganic PSCs.

To characterize the carrier lifetimes in $CsPbI_2Br$ films with varying amounts of Sb doping, time-resolved PL (TRPL) decay curves were measured for these perovskite films, as shown in Fig. 3(f). The decay times (τ) were calculated by fitting the TRPL curves with a double exponential function [39]

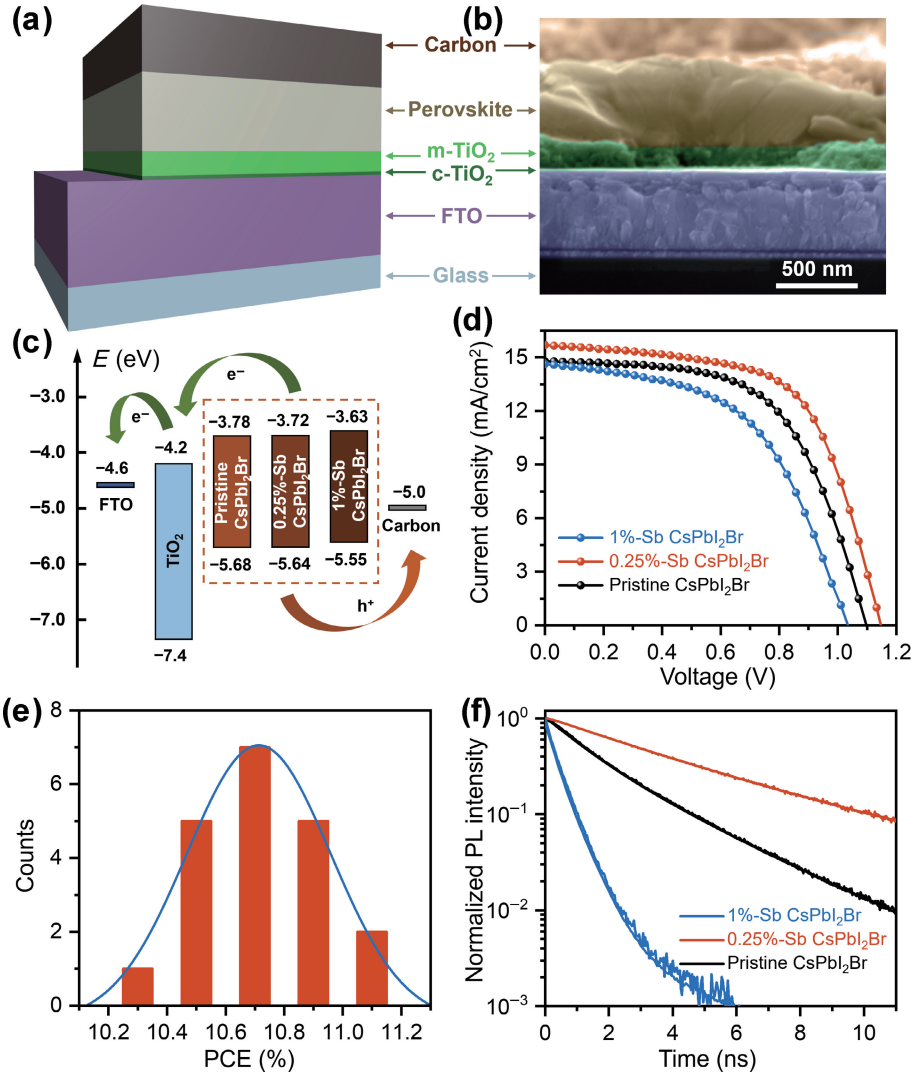

Figure 3 (a) Device configuration and (b) cross-sectional SEM image of the as-prepared HTM-free all-inorganic PSC with the structure of FTO/c-TiO_2/m-TiO_2/perovskite/nanocarbon. (c) Energy level diagram of all-inorganic PSCs with different light absorbers. (d) *J*–*V* plots of the as-prepared HTM-free all-inorganic PSCs. (e) Statistical histogram of PCEs collected from 20 individual all-inorganic PSCs based on 0.25%-Sb $CsPbI_2Br$ films. (f) TRPL spectra of pristine $CsPbI_2Br$, 0.25%-Sb $CsPbI_2Br$, and 1%-Sb $CsPbI_2Br$ films.

$$y(t) = A_1\exp(-t/\tau_1) + A_2\exp(-t/\tau_2) \quad (1)$$

where A_1 and A_2 are constants obtained from the TRPL curve fitting, t represents the lifetime, τ_1 is related to the interface recombination process, and τ_2 is attributed to the recombination process occurring inside the crystal grains. The fitting results are summarized in Table S5 in the ESM, which shows that the average carrier lifetimes of pristine $CsPbI_2Br$, 0.25%-Sb $CsPbI_2Br$, and 1%-Sb $CsPbI_2Br$ films are 2.064, 4.283, and 0.671 ns, respectively. The 0.25%-Sb $CsPbI_2Br$ film displayed a prolonged carrier lifetime, which suggests that the charge recombination process is highly inhibited and this is advantageous for improving the photovoltaic performance of the devices.

To evaluate the electron trap density (n_t), we measured the current–voltage (*I*–*V*) curves of electron-only devices in the dark state by using the space-charge-limited current (SCLC) model, as shown in Fig. S8 in the ESM. The dark *I*–*V* curves were processed using logarithms to obtain the trap-filled limit voltage (V_{TFL}), and n_t was calculated using Eq. (2) [40]

$$n_t = \frac{2\varepsilon\varepsilon_0 V_{TFL}}{eL^2} \quad (2)$$

where e is the electron charge, L is the thickness of perovskite layer, ε_0 is the vacuum dielectric constant, and ε is the relative permittivity of perovskites. The V_{TFL} of the electron-only device based on undoped $CsPbI_2Br$ film is 1.22 V, and the corresponding n_t is 9.59×10^{15} cm^{-3}. After adding 0.25% Sb^{3+}, the V_{TFL} decreased to 0.98 V, resulting in a lower density of 7.64×10^{15} cm^{-3}. The results demonstrate that Sb^{3+} doping can effectually passivate the crystal defects and inhibit charge recombination.

The influence of Sb doping on the chemical stability of $CsPbI_2Br$ based all-inorganic PSCs was assessed under different conditions. The all-inorganic PSCs based on pristine $CsPbI_2Br$ and 0.25%-Sb $CsPbI_2Br$ films were subjected to continuous heating at 60 °C in an N_2 environment. As shown in Fig. 4(a) and Fig. S9 in the ESM, the devices based on 0.25%-Sb $CsPbI_2Br$ films still maintained approximately 83% of their initial performance after heating for 450 h. In contrast, the PCE of the device based on pristine $CsPbI_2Br$ rapidly decreased to below 50% within only 300 h of continuous heating. Even in ambient conditions, the devices based on 0.25%-Sb $CsPbI_2Br$ films exhibited superior thermal stability. After subjecting the encapsulated PSCs to continuous heating at 60 °C for a week, the devices based on 0.25%-Sb $CsPbI_2Br$ films retained 89% of their initial PCE, in contrast to the rapid degradation observed in pristine $CsPbI_2Br$-based devices, as presented in Fig. 4(b) and Fig. S10 in the ESM. When exposed to an ambient environment at 60 °C without encapsulation under a relative humidity (RH) of 30%, the PSCs based on 0.25%-Sb $CsPbI_2Br$ films maintained 88% of the initial

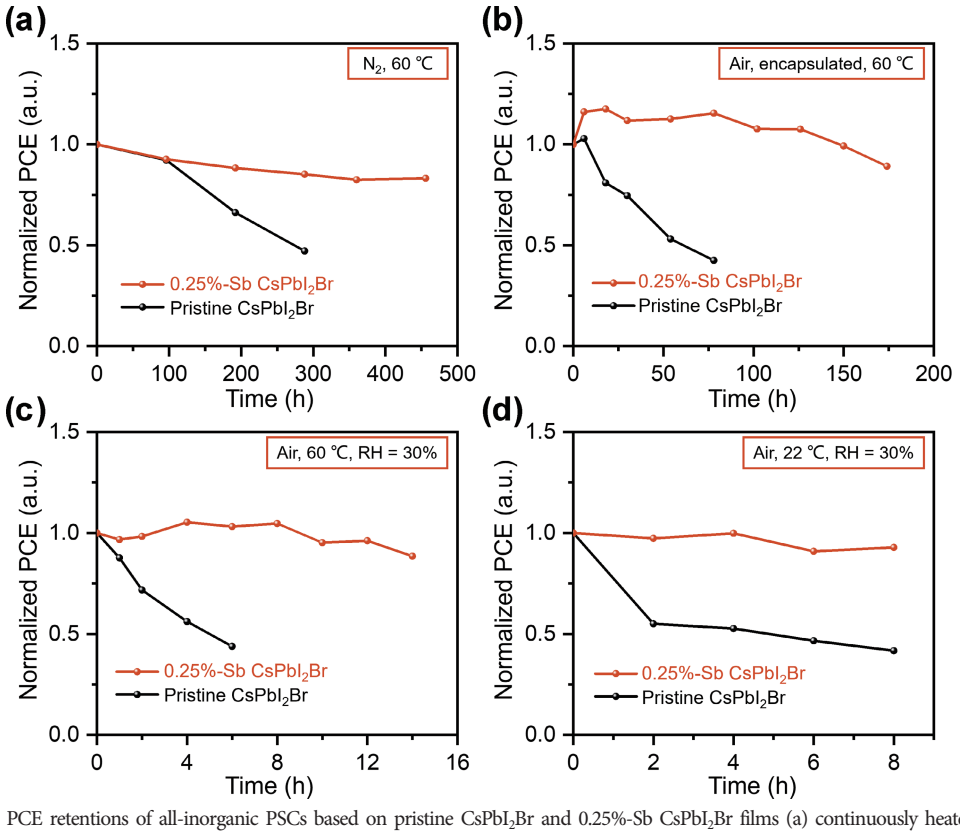

Figure 4 Normalized PCE retentions of all-inorganic PSCs based on pristine $CsPbI_2Br$ and 0.25%-Sb $CsPbI_2Br$ films (a) continuously heated at 60 °C under N_2 atmosphere without encapsulation, (b) continuously heated at 60 °C in an ambient environment with encapsulation, (c) continuously heated at 60 °C in an ambient environment without encapsulation, and (d) exposed to air (RH = 30%) at room temperature (22 °C) without encapsulation, respectively.

PCE after a continuous exposure period of 14 h. In contrast, pristine $CsPbI_2Br$-based devices exhibited rapid degradation, with only 44% of the initial PCE retained after just 6 h, as presented in Fig. 4(c) and Fig. S11 in the ESM. Additionally, the moisture resistance of all-inorganic PSCs based on 0.25%-Sb $CsPbI_2Br$ was evaluated at room temperature (22 °C). Exposure to humid air with an RH of 30% at room temperature resulted in rapid degradation of unencapsulated pristine $CsPbI_2Br$ devices, which exhibited only about 42% of the initial PCE after 8 h. Conversely, the devices based on 0.25%-Sb $CsPbI_2Br$ films retained 92% of the initial PCE after the same duration (Fig. 4(d) and Fig. S12 in the ESM), and still maintained approximately 45% of the initial value even after prolonged exposure to humid air for up to 66 h (Fig. S13 in the ESM). Figure S14 in the ESM illustrates the stability of PSCs in an N_2 environment at room temperature, where the devices based on pristine $CsPbI_2Br$ and 0.25%-Sb $CsPbI_2Br$ films both maintained over 70% of their initial PCE even after an extended exposure period of up to 1200 h. Figure S15 in the ESM shows the stability of the encapsulated PSCs in ambient environment. Compared to pristine $CsPbI_2Br$-based devices, all-inorganic PSCs based on 0.25%-Sb $CsPbI_2Br$ films demonstrated greatly improved environmental stability. Collectively, these results demonstrate that the incorporation of Sb^{3+} can significantly enhance the heat and moisture tolerances of all-inorganic PSCs based on $CsPbI_2Br$. The exceptional thermal and humidity stabilities observed in the devices could be attributed to the doping of Sb, which can help maintain a stable $CsPbI_2Br$ crystal structure even at high temperatures. The incorporation of Sb will reduce the size of the $[BX_6]$ structure and decrease lattice constant, which improves matching between octahedral voids and Cs cations, thereby maintaining the structural integrity of $CsPbI_2Br$ [41]. On the other hand, the degree of resistance to heat or humidity can also be attributed to fewer defects in the perovskite structure resulted from Sb doping.

The hysteresis characteristics of all-inorganic PSCs based on pristine $CsPbI_2Br$ and 0.25%-Sb $CsPbI_2Br$ films were compared by measuring their J–V curves using forward and reverse scanning modes, as depicted in Fig. S16 in the ESM. The hysteresis index (HI) can be calculated using Eq. (3) [42]

$$HI = (PCE_R - PCE_F)/PCE_R \quad (3)$$

where R and F represent the reverse scan and forward scan, respectively. The calculation results of the HI value were summarized in Table S6 in the ESM. It indicates that the pristine $CsPbI_2Br$ device exhibited significant hysteresis, with an HI value as high as 13.61%. In contrast, the incorporation of 0.25%-Sb into $CsPbI_2Br$ films effectively suppressed hysteresis, with the resulting device exhibiting an HI value of only 5.37%. This improvement in hysteresis suppression could be attributed to the fact that an appropriate amount of Sb doping can reduce trap states within the film, thereby inhibiting charge recombination [43].

The charge transfer characteristics of PSCs were analyzed using electrochemical impedance spectroscopy (EIS) measurements. The results of these EIS measurements with the equivalent circuit are presented in Fig. S17 in the ESM. The fitting parameters obtained from the EIS measurements are summarized in Table S7 in the ESM. Typically, the arc observed in the high frequency region represents a transport process that combines charge transport resistance and chemical capacitance (C_{rec}), corresponding to the series resistance (R_s) from cathode to anode. Meanwhile, the arc observed at low frequencies is related to recombination resistance (R_{rec}) and C_{rec} of the device [44]. Due to the same device architecture, both samples exhibited very similar series resistance. However, the devices based on 0.25%-Sb $CsPbI_2Br$ films displayed a higher R_{rec} value, indicating that charge recombination was significantly inhibited in this material [45, 46]. This observation is consistent with the higher V_{OC} value and reduced hysteresis observed in the devices based on 0.25%-Sb

$CsPbI_2Br$ films.

3 Conclusions

In summary, this work successfully incorporated Sb^{3+} into the $CsPbI_2Br$ perovskite structures by the partial substitution of Pb^{2+} with Sb^{3+} at B-sites. The Sb doping effectively improved phase stability and resulted in a denser perovskite film structure with fewer defects and longer carrier lifetime. Compared to carbon-based PSCs based on pristine $CsPbI_2Br$, all-inorganic PSCs based on 0.25%-Sb $CsPbI_2Br$ exhibited an enhanced PCE of 11.06%, with greatly reduced hysteresis, good thermal stability, and moisture resistance. By utilizing screen-printable inorganic carbon electrodes instead of organic HTMs and noble metal electrodes, the stability of the device can be significantly increased, meanwhile greatly reducing the complexity and cost associated with device manufacturing. This study is expected to promote further research and practical applications of all-inorganic PSCs with high stability and low fabrication cost.

Acknowledgements

The authors are grateful to the support of the National Key R&D Program of China (No. 2017YFA0208200), the National Natural Science Foundation of China (Nos. 22022505 and 21872069), the Fundamental Research Funds for the Central Universities (Nos. 020514380266, 020514380272, and 020514380274), the Scientific and Technological Innovation Special Fund for Carbon Peak and Carbon Neutrality of Jiangsu Province (No. BK20220008), the Nanjing International Collaboration Research Program (Nos. 202201007 and 2022SX00000955), and the Suzhou Gusu Leading Talent Program of Science and Technology Innovation and Entrepreneurship in Wujiang District (No. ZXL2021273).

Electronic Supplementary Material: Supplementary material (additional experimental details and data, including experimental methods, XRD patterns, high-resolution XPS spectra, SEM images, EDX mappings, UV–Vis absorption spectra, stability tests, *J*–*V* plots, Nyquist plots, and photovoltaic performances (Figs. S1–S17 and Tables S1–S7 in the ESM)) is available in the online version of this article at https://doi.org/10.1007/s12274-023-5981-7.

References

[1] Burschka, J.; Pellet, N.; Moon, S. J.; Humphry-Baker, R.; Gao, P.; Nazeeruddin, M. K.; Grätzel, M. Sequential deposition as a route to high-performance perovskite-sensitized solar cells. *Nature* **2013**, *499*, 316–319.

[2] Kim, H. S.; Lee, C. R.; Im, J. H.; Lee, K. B.; Moehl, T.; Marchioro, A.; Moon, S. J.; Humphry-Baker, R.; Yum, J. H.; Moser, J. E. et al. Lead iodide perovskite sensitized all-solid-state submicron thin film mesoscopic solar cell with efficiency exceeding 9%. *Sci. Rep.* **2012**, *2*, 591.

[3] Zhou, H. P.; Chen, Q.; Li, G.; Luo, S.; Song, T. B.; Duan, H. S.; Hong, Z. R.; You, J. B.; Liu, Y. S.; Yang, Y. Interface engineering of highly efficient perovskite solar cells. *Science* **2014**, *345*, 542–546.

[4] Chen, W.; Wu, Y. Z.; Yue, Y. F.; Liu, J.; Zhang, W. J.; Yang, X. D.; Chen, H.; Bi, E. B.; Ashraful, I.; Grätzel, M. et al. Efficient and stable large-area perovskite solar cells with inorganic charge extraction layers. *Science* **2015**, *350*, 944–948.

[5] Kojima, A.; Teshima, K.; Shirai, Y.; Miyasaka, T. Organometal halide perovskites as visible-light sensitizers for photovoltaic cells. *J. Am. Chem. Soc.* **2009**, *131*, 6050–6051.

[6] Park, J.; Kim, J.; Yun, H. S.; Paik, M. J.; Noh, E.; Mun, H. J.; Kim, M. G.; Shin, T. J.; Seok, S. I. Controlled growth of perovskite layers with volatile alkylammonium chlorides. *Nature* **2023**, *616*, 724–730.

[7] NREL. *Best Research-Cell Efficiency Chart* [Online]. https://www.nrel.gov/pv/cell-efficiency.html (accessed Apr 25, 2023).

[8] Kim, N. K.; Min, Y. H.; Noh, S.; Cho, E.; Jeong, G.; Joo, M.; Ahn, S. W.; Lee, J. S.; Kim, S.; Ihm, K. et al. Investigation of thermally induced degradation in $CH_3NH_3PbI_3$ perovskite solar cells using *in-situ* synchrotron radiation analysis. *Sci. Rep.* **2017**, *7*, 4645.

[9] Yang, W. S.; Park, B. W.; Jung, E. H.; Jeon, N. J.; Kim, Y. C.; Lee, D. U.; Shin, S. S.; Seo, J.; Kim, E. K.; Noh, J. H. et al. Iodide management in formamidinium-lead-halide-based perovskite layers for efficient solar cells. *Science* **2017**, *356*, 1376–1379.

[10] Wang, Z.; Shi, Z. J.; Li, T. T.; Chen, Y. H.; Huang, W. Stability of perovskite solar cells: A prospective on the substitution of the A cation and X anion. *Angew. Chem., Int. Ed.* **2017**, *56*, 1190–1212.

[11] Jeon, N. J.; Na, H.; Jung, E. H.; Yang, T. Y.; Lee, Y. G.; Kim, G.; Shin, H. W.; Seok, S. I.; Lee, J.; Seo, J. A fluorene-terminated hole-transporting material for highly efficient and stable perovskite solar cells. *Nat. Energy* **2018**, *3*, 682–689.

[12] Liang, J.; Wang, C. X.; Wang, Y. R.; Xu, Z. R.; Lu, Z. P.; Ma, Y.; Zhu, H. F.; Hu, Y.; Xiao, C. C.; Yi, X. et al. All-inorganic perovskite solar cells. *J. Am. Chem. Soc.* **2016**, *138*, 15829–15832.

[13] Zhou, G.; Wu, J. H.; Zhao, Y. H.; Li, Y. M.; Shi, J. J.; Li, Y. S.; Wu, H. J.; Li, D. M.; Luo, Y. H.; Meng, Q. B. Application of cesium on the restriction of precursor crystallization for highly reproducible perovskite solar cells exceeding 20% efficiency. *ACS Appl. Mater. Interfaces* **2018**, *10*, 9503–9513.

[14] Ding, L. M.; Cheng, Y. B.; Tang, J. $CsPb_{0.9}Sn_{0.1}IBr_2$ based all-inorganic perovskite solar cells exhibit improved efficiency and stability. *Acta Phys. Chim. Sin.* **2018**, *34*, 449–450.

[15] Lin, J.; Lai, M. L.; Dou, L. T.; Kley, C. S.; Chen, H.; Peng, F.; Sun, J. L.; Lu, D.; Hawks, S. A.; Xie, C. L. et al. Thermochromic halide perovskite solar cells. *Nat. Mater.* **2018**, *17*, 261–267.

[16] Nam, J. K.; Chun, D. H.; Rhee, R. J. K.; Lee, J. H.; Park, J. H. Methodologies toward efficient and stable cesium lead halide perovskite-based solar cells. *Adv. Sci.* **2018**, *5*, 1800509.

[17] Kulbak, M.; Gupta, S.; Kedem, N.; Levine, I.; Bendikov, T.; Hodes, G.; Cahen, D. Cesium enhances long-term stability of lead bromide perovskite-based solar cells. *J. Phys. Chem. Lett.* **2016**, *7*, 167–172.

[18] Zhang, Y. L.; Luo, L.; Hua, J. C.; Wang, C.; Huang, F. Z.; Zhong, J.; Peng, Y.; Ku, Z. L.; Cheng, Y. B. Moisture assisted $CsPbBr_3$ film growth for high-efficiency, all-inorganic solar cells prepared by a multiple sequential vacuum deposition method. *Mater. Sci. Semicond. Process.* **2019**, *98*, 39–43.

[19] Frolova, L. A.; Anokhin, D. V.; Piryazev, A. A.; Luchkin, S. Y.; Dremova, N. N.; Stevenson, K. J.; Troshin, P. A. Highly efficient all-inorganic planar heterojunction perovskite solar cells produced by thermal coevaporation of CsI and PbI_2. *J. Phys. Chem. Lett.* **2017**, *8*, 67–72.

[20] Liang, J.; Han, X.; Yang, J. H.; Zhang, B. Y.; Fang, Q. Y.; Zhang, J.; Ai, Q.; Ogle, M. M.; Terlier, T.; Martí, A. A. et al. Defect-engineering-enabled high-efficiency all-inorganic perovskite solar cells. *Adv. Mater.* **2019**, *31*, 1903448.

[21] Sutton, R. J.; Eperon, G. E.; Miranda, L.; Parrott, E. S.; Kamino, B. A.; Patel, J. B.; Hörantner, M. T.; Johnston, M. B.; Haghighirad, A. A.; Moore, D. T. et al. Bandgap-tunable cesium lead halide perovskites with high thermal stability for efficient solar cells. *Adv. Energy Mater.* **2016**, *6*, 1502458.

[22] Liang, J.; Liu, J.; Jin, Z. All-inorganic halide perovskites for optoelectronics: Progress and prospects. *Sol. RRL* **2017**, *1*, 1700086.

[23] Liu, C.; Li, W. Z.; Zhang, C. L.; Ma, Y. P.; Fan, J. D.; Mai, Y. H. All-inorganic $CsPbI_2Br$ perovskite solar cells with high efficiency exceeding 13%. *J. Am. Chem. Soc.* **2018**, *140*, 3825–3828.

[24] Sun, H. R.; Zhang, J.; Gan, X. L.; Yu, L. T.; Yuan, H. B.; Shang, M. H.; Lu, C. J.; Hou, D. G.; Hu, Z. Y.; Zhu, Y. J. et al. Pb-reduced $CsPb_{0.9}Zn_{0.1}I_2Br$ thin films for efficient perovskite solar cells. *Adv. Energy Mater.* **2019**, *9*, 1900896.

[25] Lau, C. F. J.; Zhang, M.; Deng, X. F.; Zheng, J. H.; Bing, J. M.; Ma, Q. S.; Kim, J.; Hu, L.; Green, M. A.; Huang, S. J. et al. Strontium-doped low-temperature-processed $CsPbI_2Br$ perovskite solar cells. *ACS Energy Lett.* **2017**, *2*, 2319–2325.

[26] Liang, J.; Liu, Z. H.; Qiu, L. B.; Hawash, Z.; Meng, L. Q.; Wu, Z. F.; Jiang, Y.; Ono, L. K.; Qi, Y. B. Enhancing optical, electronic, crystalline, and morphological properties of cesium lead halide by

Mn substitution for high-stability all-inorganic perovskite solar cells with carbon electrodes. *Adv. Energy Mater.* **2018**, *8*, 1800504.

[27] Liu, C.; Li, W. Z.; Li, H. Y.; Wang, H. M.; Zhang, C. L.; Yang, Y. G.; Gao, X. Y.; Xue, Q. F.; Yip, H. L.; Fan, J. D. et al. Structurally reconstructed $CsPbI_2Br$ perovskite for highly stable and square-centimeter all-inorganic perovskite solar cells. *Adv. Energy Mater.* **2019**, *9*, 1803572.

[28] Yuan, H. W.; Zhao, Y. Y.; Duan, J. L.; Wang, Y. D.; Yang, X. Y.; Tang, Q. W. All-inorganic $CsPbBr_3$ perovskite solar cell with 10.26% efficiency by spectra engineering. *J. Mater. Chem. A* **2018**, *6*, 24324–24329.

[29] Etgar, L.; Gao, P.; Xue, Z. S.; Peng, Q.; Chandiran, A. K.; Liu, B.; Nazeeruddin, M. K.; Grätzel, M. Mesoscopic $CH_3NH_3PbI_3/TiO_2$ heterojunction solar cells. *J. Am. Chem. Soc.* **2012**, *134*, 17396–17399.

[30] Mei, A. Y.; Li, X.; Liu, L. F.; Ku, Z. L.; Liu, T. F.; Rong, Y. G.; Xu, M.; Hu, M.; Chen, J. Z.; Yang, Y. et al. A hole-conductor-free, fully printable mesoscopic perovskite solar cell with high stability. *Science* **2014**, *345*, 295–298.

[31] Christodoulou, S.; Di Stasio, F.; Pradhan, S.; Stavrinadis, A.; Konstantatos, G. High-open-circuit-voltage solar cells based on bright mixed-halide $CsPbBrI_2$ perovskite nanocrystals synthesized under ambient air conditions. *J. Phys. Chem. C* **2018**, *122*, 7621–7626.

[32] Kim, M.; Kim, G. H.; Oh, K. S.; Jo, Y.; Yoon, H.; Kim, K. H.; Lee, H.; Kim, J. Y.; Kim, D. S. High-temperature-short-time annealing process for high-performance large-area perovskite solar cells. *ACS Nano* **2017**, *11*, 6057–6064.

[33] Chai, W. M.; Zhu, W. D.; Zhang, Z. Y.; Liu, D. W.; Ni, Y. F.; Song, Z. C.; Dong, P.; Chen, D. Z.; Zhang, J. C.; Zhang, C. F. et al. $CsPbBr_3$ seeds improve crystallization and energy level alignment for highly efficient $CsPbI_3$ perovskite solar cells. *Chem. Eng. J.* **2023**, *452*, 139292.

[34] Lau, C. F. J.; Deng, X. F.; Zheng, J. H.; Kim, J.; Zhang, Z. L.; Zhang, M.; Bing, J. M.; Wilkinson, B.; Hu, L.; Patterson, R. et al. Enhanced performance via partial lead replacement with calcium for a $CsPbI_3$ perovskite solar cell exceeding 13% power conversion efficiency. *J. Mater. Chem. A* **2018**, *6*, 5580–5586.

[35] Chung, I.; Lee, B.; He, J. Q.; Chang, R. P. H.; Kanatzidis, M. G. All-solid-state dye-sensitized solar cells with high efficiency. *Nature* **2012**, *485*, 486–489.

[36] Zhang, J.; Shang, M. H.; Wang, P.; Huang, X. K.; Xu, J.; Hu, Z. Y.; Zhu, Y. J.; Han, L. Y. n-Type doping and energy states tuning in $CH_3NH_3Pb_{1-x}Sb_{2x/3}I_3$ perovskite solar cells. *ACS Energy Lett.* **2016,** *1*, 535–541.

[37] Xiang, S. S.; Li, W. P.; Wei, Y.; Liu, J. M.; Liu, H. C.; Zhu, L. Q.; Chen, H. N. The synergistic effect of non-stoichiometry and Sb-doping on air-stable alpha-$CsPbI_3$ for efficient carbon-based perovskite solar cells. *Nanoscale* **2018**, *10*, 9996–10004.

[38] Brandt, R. E.; Stevanović, V.; Ginley, D. S.; Buonassisi, T. Identifying defect-tolerant semiconductors with high minority-carrier lifetimes: Beyond hybrid lead halide perovskites. *MRS Commun.* **2015**, *5*, 265–275.

[39] Xia, Y. R.; Zhao, C.; Zhao, P. Y.; Mao, L. Y.; Ding, Y. C.; Hong, D. C.; Tian, Y. X.; Yan, W. S.; Jin, Z. Pseudohalide substitution and potassium doping in $FA_{0.98}K_{0.02}Pb(SCN)_2I$ for high-stability hole-conductor-free perovskite solar cells. *J. Power Sources* **2021**, *494*, 229781.

[40] Zhu, M. F.; Xia, Y. R.; Qin, L. N.; Zhang, K. Q.; Liang, J. C.; Zhao, C.; Hong, D. C.; Jiang, M. H.; Song, X. M.; Wei, J. et al. Reducing surficial and interfacial defects by thiocyanate ionic liquid additive and ammonium formate passivator for efficient and stable perovskite solar cells. *Nano Res.* **2023**, *16*, 6849–6858.

[41] Li, Z.; Yang, M. J.; Park, J. S.; Wei, S. H.; Berry, J. J.; Zhu, K. Stabilizing perovskite structures by tuning tolerance factor: Formation of formamidinium and cesium lead iodide solid-state alloys. *Chem. Mater.* **2016**, *28*, 284–292.

[42] Xia, Y. R.; Zhu, M. F.; Qin, L. N.; Zhao, C.; Hong, D. C.; Tian, Y. X.; Yan, W. S.; Jin, Z. Organic–inorganic hybrid quasi-2D perovskites incorporated with fluorinated additives for efficient and stable four-terminal tandem solar cells. *Energy Mater.* **2023**, *3*, 300004.

[43] Lee, J. W.; Kim, S. G.; Bae, S. H.; Lee, D. K.; Lin, O.; Yang, Y.; Park, N. G. The interplay between trap density and hysteresis in planar heterojunction perovskite solar cells. *Nano. Lett.* **2017**, *17*, 4270–4276.

[44] Ma, J. J.; Yang, G.; Qin, M. C.; Zheng, X. L.; Lei, H. W.; Chen, C.; Chen, Z. L.; Guo, Y. X.; Han, H. W.; Zhao, X. Z. et al. MgO nanoparticle modified anode for highly efficient SnO_2-based planar perovskite solar cells. *Adv. Sci.* **2017**, *4*, 1700031.

[45] Yang, F.; Hirotani, D.; Kapil, G.; Kamarudin, M. A.; Ng, C. H.; Zhang, Y. H.; Shen, Q.; Hayase, S. All-inorganic $CsPb_{1-x}Ge_xI_2Br$ perovskite with enhanced phase stability and photovoltaic performance. *Angew. Chem., Int. Ed.* **2018**, *57*, 12745–12749.

[46] Guo, Z. L.; Zhao, S.; Liu, A. M.; Kamata, Y.; Teo, S.; Yang, S. Z.; Xu, Z. H.; Hayase, S.; Ma, T. L. Niobium incorporation into $CsPbI_2Br$ for stable and efficient all-inorganic perovskite solar cells. *ACS Appl. Mater. Interfaces* **2019**, *11*, 19994–20003.